Integrating Materials and Manufacturing Innovation (2019) 8:178–193
https://doi.org/10.1007/s40192-019-00130-x

THEMATIC SECTION: ADDITIVE MANUFACTURING BENCHMARKS 2018

Benchmark Study of Thermal Behavior, Surface Topography, and Dendritic Microstructure in Selective Laser Melting of Inconel 625

Zhengtao Gan[1] · Yanping Lian[2] · Stephen E. Lin[1] · Kevontrez K. Jones[1] · Wing Kam Liu[1] · Gregory J. Wagner[1]

Received: 14 January 2019 / Accepted: 18 March 2019 / Published online: 12 April 2019

Abstract

In the NIST additive manufacturing benchmark (AM-Bench) experiments, melt pool geometry, cooling rates, surface topography, and dendritic microstructure in laser melted Inconel 625 were used to challenge and validate computational models of the melting and solidification process. To this end, three thermal models incorporating different physics are compared with the experimental data. It is identified that the heat convection enhanced by the thermocapillary flow inside the melt pool and heat loss caused by vaporization play pivotal roles to guarantee the accuracy of the predictions, and thus should be considered in the thermal model. Neglecting fluid flow and vaporization leads to nearly 100% difference in cooling rate during solidification, and 20% difference in cooling rate after solidification from the results. With the most accurate thermal model, surface topographies of the melt tracks are predicted and quantitatively analyzed. Using the Kurz-Fisher model, the primary dendrite arm spacing is predicted based on the thermal gradient and solidification rate predictions, while elemental segregation is predicted using the Scheil-Gulliver model and a non-equilibrium solidification model. Additionally, it is shown that increasing scan speed inhibits elemental microsegregation.

Keywords Additive manufacturing · Fluid flow · Cooling rate · Dendrite arm spacing · Microsegregation · Ni-based superalloy

Introduction

Metallic additive manufacturing, including laser/electron beam powder bed fusing (L/E-PBF) and directed energy deposition (DED), provides opportunities to reduce the cost of manufacturing Ni/Ti-based superalloy parts, especially with complex geometries such as internal cooling channels for high-temperature applications [1–3]. However, inappropriate process parameters lead to defects, such as lack of fusion [4], porosity [5], low surface quality [6], cracking [7], and precipitation of brittle phases [8], which degrade mechanical properties. Finding suitable process parameters for manufacturing and heat treatment processes through trial and error is time-consuming. Predictive modeling can help accelerate this search.

Computational modeling has been crucial to understanding process–structure–properties linkages in additive manufacturing (AM) [9]. To assess the highly transient manufacturing process, finite element/volume method-based thermal models have been developed. Using a heat conduction model, thermal and cooling behaviors of deposited Fe-TiC composite during laser cladding were studied by Emamian et al. [10]. Gao et al. [11] developed a 3D thermal model using the finite element method (FEM) to calculate the thermal gradient and the solidification rate at the liquid–solid interface of an Fe-based alloy. A thermodynamically consistent model has been proposed to evaluate microstructure based on thermal behavior during the process [12]. However, fluid flow inside the melt pool was not considered in these aforementioned numerical models, and thus neglected to directly incorporate the effects of cooling through fluid

Zhengtao Gan and Yanping Lian contributed equally to this work.

✉ Wing Kam Liu
w-liu@northwestern.edu

✉ Gregory J. Wagner
gregory.wagner@northwestern.edu

[1] Department of Mechanical Engineering, Northwestern University, Evanston, IL 60208, USA

[2] Institute of Advanced Structure Technology, Beijing Institute of Technology, Beijing, 100081, China

convection. Several thermal-fluid flow models, which consider liquid metal flow within the melt pool, have also been developed. DebRoy's group developed heat transfer and fluid flow models in welding and additive manufacturing [13–15]. Flat surface assumptions have been made to simplify the problems. A few multiphase flow models have been proposed to consider free surface evolution using the Level-Set (LS) [16, 17] or Volume of Fluid (VOF) [18, 19] methods. The addition of free surface capturing or tracking enables powder scale simulation and a better resolution of the inter-facial forces [20, 21].

To predict microstructure and phase formation of additively manufactured materials, several microstructure models have been developed. Cellular automaton (CA) [22] and kinetic Monte Carlo (KMC) [23] models have been utilized to predict grain structure evolution in additive manufacturing. For predicting dendrite formation and morphology during solidification, phase field methods have been developed for binary and multicomponent alloys [2, 24]. Based on CALculation of PHAse Diagrams (CALPHAD), elemental segregation can be evaluated in thermodynamic equilibrium [25] and non-equilibrium [26] processes.

However, ensuring the accuracy of the models mentioned above requires well-designed and highly controlled experiments for validation. Because of the extremely high temperature, metallic powder spattering, and multiple physical scales presenting in the melt pool, it has been difficult to conduct in situ measurements of the variables of interest. Typically, ex situ measurements are used to detect the fusion boundary at the cross section of fabricated samples that is used for numerical validation [27]. By using Electron Backscatter Diffraction (EBSD) [28] and Scanning Electron Microscope (SEM) imaging [29], the grain and dendritic microstructure can be obtained from sample cross sections. Recently, in situ observation techniques have been proposed to conduct time-resolved measurements for the melt pool length [30], cooling rate [31], powder spatter [32], and phase transformation [33] enabling the design of highly controlled experiments. In February 2018, the United States National Institute of Standards and Technology (NIST) laboratory announced the Additive Manufacturing Benchmarks 2018 (AM-Bench), which provided a series of highly controlled additive manufacturing benchmark tests and asked for model predictions around the world for quantitative validation [34]. Model predictions were submitted by the May 18, 2018. All experimental results were released on May 19, 2018. These experiments challenge participants to address the problem of AM modeling, and allow the validation of different numerical models to explore the impacts including detailed physical phenomena and microscale information on accuracy and efficiency.

This paper describes a simulation effort to model one set of AM-Bench experiments, measuring process behavior and material microstructure for individual laser tracks on Inconel 625 bare substrates. The melt pool dimensions, cooling rate, surface topography, primary dendrite arm spacing, and elemental microsegregation are explored in detail. The rest of the paper is organized as follows: In "Experimental Methods," the experimental methods for AM-Bench are briefly described. In "Computational Models," the computational methods are provided in detail. In "Results and Discussion," the detailed comparison of the experimental data and simulation results are presented. Finally, conclusions and perspectives are discussed in "Conclusions."

Experimental Methods

At NIST, an EOS M270, which is referred to the Commercial Build Machine (CBM), was used to produce multiple single-track scans. A 1070-nm continuous wave laser with a beam diameter of 100 μm at its focus melted an Inconel 625 (IN625) bare plate (no powder). In this work, the beam diameter is defined as the width of the beam at which the Gaussian beam intensity has fallen to $1/e^2$ ($\sim$13.5%) of its peak. Low-velocity gas flow consisted of Nitrogen and 0.5% Oxygen. Three different cases were conducted: case A of laser power of 150 W and scan speed of 400 mm/s, case B of laser power of 195 W and scan speed of 800 mm/s, and case C of laser power of 195 W and scan speed of 1200 mm/s. High-speed short-wave infrared cameras (SWIR) were used for in situ measurements of the melt pool length and cooling rates while laser scanning confocal microscopy was used for the characterization of 3D topographies of the top surfaces of laser tracks. Cross-sectional geometry and microstructure were obtained using optical microscopy and scanning electron microscopy (SEM) with secondary electron (SE) imaging, electron backscatter diffraction (EBSD), and energy dispersive spectroscopy (EDS). More detailed information of the experimental setups and measurements are available on the AM-Bench website [35].

Computational Models

A framework of integrated computational models is proposed for the AM-Bench experiments and shown in Fig. 1. To predict the melt pool geometry and cooling rates during the process, three thermal models considering varying levels of physics were developed for comparison: (1) heat conduction model solving the thermal diffusion

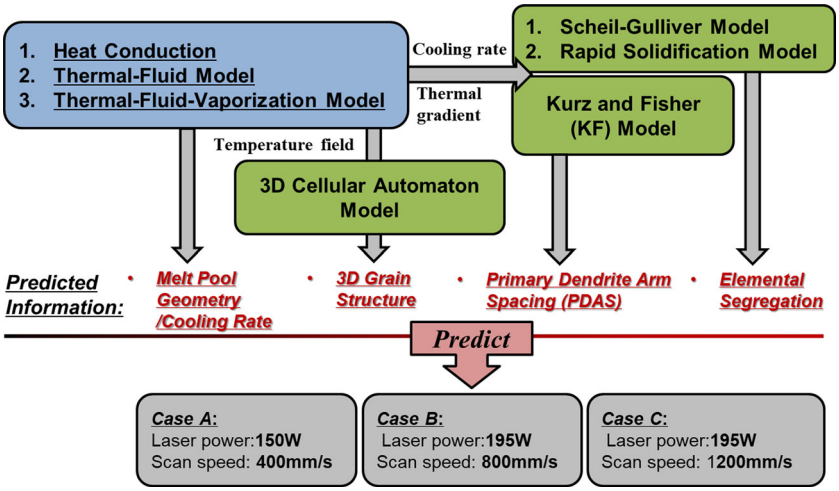

Fig. 1 A flowchart including computational models, predicted information, and three cases with different process parameters

equation, (2) thermal-fluid model considering liquid flow inside the melt pool driven by Marangoni effect, and (3) thermal-fluid-vaporization model further considering heat loss caused by vaporization. Based on the cooling rate and thermal gradient obtained from the most accurate thermal model, primary dendrite arm spacing can be predicted using the Kurz-Fisher (KF) model [36] with experimental calibration. In addition, elemental segregation is evaluated based on two CALPHAD-based models: (1) the Scheil-Gulliver model [37] with a thermodynamic equilibrium assumption and (2) a non-equilibrium solidification model for multicomponent alloys [26]. To predict 3D grain structures, a 3D cellular automaton (CA) model [22] was developed for additive manufacturing and allows simulations of a large numbers of grains within domains at the millimeter scale and beyond; details of the CA model are not the focus of this paper.

Thermal-Fluid-Vaporization Model

Since the thermal-fluid-vaporization model [38] can be reduced to others models mentioned above, we presented it only in this section. The model is simplified based on several following assumptions [39]:

1. The densities of the liquid and solid metals are treated as constant within each phase (though not necessarily across phase interfaces).
2. The thermocapillary flow inside the melt pool is assumed to be incompressible and laminar with a Boussinesq approximation of buoyancy effect.
3. The solid substrate is treated as a Newtonian fluid with a very large viscosity, and the strain and stress in the solid are neglected.
4. Mass loss and composition change due to vaporization are neglected.
5. Flow in the mushy zone is assumed to be described as that in an isotropic porous medium, with permeability given by the Carmen-Kozeny relation [40].
6. Viscous dissipation is neglected in the energy equation.

Under the assumptions above, the governing equations for mass, momentum, and energy conservation are given as follows [27]:

$$\frac{\partial \rho}{\partial t} + \frac{\partial \rho u_i}{\partial x_i} = 0 \tag{1}$$

$$\frac{\partial \rho u_i}{\partial t} + \frac{\partial \rho u_i u_j}{\partial x_j} = \frac{\partial}{\partial x_j}(\mu(\frac{\partial u_i}{\partial x_j})) - \frac{\partial p}{\partial x_i} - \frac{180\mu}{\delta^2}\frac{(1-f_l)^2}{f_l^3 + B}u_i + \rho_{ref} g_i \beta (T - T_{ref}) \tag{2}$$

$$\frac{\partial \rho h}{\partial t} + \frac{\partial \rho u_i h}{\partial x_i} = \frac{\partial}{\partial x_i}(k\frac{\partial T}{\partial x_i}) \tag{3}$$

where t is the time, u_i is the ith component of the velocity, μ is the viscosity, p is the pressure, h is the enthalpy, T is the temperature, ρ is the density, k is the thermal conductivity and β is the thermal expansion coefficient. In this study, μ is set as a constant, δ is approximate primary dendritic spacing, which is set to 1 μm, B is a small parameter to avoid division by zero and set to 10^{-3}. The relationship between enthalpy and temperature to close the equation set is

$$\rho h = \int_0^T \rho c_p dT' + \rho L f_l \tag{4}$$

where c_p is the specific heat capacity, L is the latent enthalpy of fusion, and f_l is the volume fraction of liquid phase.

The thermal boundary condition including the heat source model at the liquid-gas interface is specified as:

$$q_{ener} = \frac{2Q\eta}{\pi r_b^2}\exp\left(\frac{-2((x-V_s t)^2+y^2)}{r_b^2}\right) - h_c(T-T_\infty) - \sigma_s\varepsilon(T^4-T_{ref}^4) - \sum_{i=1}^{n} J_i \Delta H_i \quad (5)$$

where Q is the laser power, η is the absorptivity, r_b is the laser beam radius, V_s is the scanning speed, h_c is the convective heat transfer coefficient, T_∞ is the ambient temperature, σ_s is the Stefan−Boltzmann constant, ε is the emissivity, T_{ref} is the reference temperature, ΔH_i is the vaporization latent heat of element i, n is the number of elements, and J_i is the vaporization rate of element i. The Langmuir equation [41] is applied to evaluate J_i as follows:

$$J_i = \frac{\chi P_i}{\sqrt{2\pi M_i RT}} \quad (6)$$

Here, P_i is the vapor pressure of element i, M_i is the molecular weight of the element i, R is the gas constant, and χ is a positive constant that accounts for the condensation of a portion of the vaporized atoms at atmospheric pressure. χ is 0.1 in this case [41].

The boundary condition for Eq. 2 at the liquid–gas interface is:

$$F_{L/G} = \gamma \boldsymbol{n}\kappa + \nabla_S T\frac{d\gamma}{dT} \quad (7)$$

where γ is the surface tension coefficient, $\boldsymbol{n}$ is the outward pointing normal of the surface, and κ is the curvature of the surface.

To predict the topology of the free surface of the melt pool, the liquid–gas interface profile is calculated by minimizing the total energy of the surface defined as

$$E = \iint_S \left(\gamma\sqrt{1+\left(\frac{\partial\phi}{\partial x}\right)^2+\left(\frac{\partial\phi}{\partial y}\right)^2} + \frac{1}{2}\rho g\phi^2 - 2\mu\frac{\partial \boldsymbol{u}}{\partial n}\boldsymbol{n}\phi - P_r\phi\right)\mathrm{d}x\,\mathrm{d}y \quad (8)$$

where ϕ is the depression of free surface, and P_r is the recoil pressure due to vaporization. The four terms on right hand side of Eq. 8 are energetic contributions due to the surface curvature, gravitational potential energy, convection, and recoil pressure, respectively. The recoil pressure is calculated from the Clausius-Clapeyron equation [42] as

$$P_r(T) \cong 0.54 P_{sat}(T) = 0.54 P_0 \exp\left(L_v\frac{T-T_b}{RTT_b}\right) \quad (9)$$

Here, P_{sat} is the saturation pressure at the boiling temperature T_b, P_0 is the atmospheric pressure, L_v is the latent heat of vaporization, and R is the gas constant. The thermal properties and compositions of IN625 are summarized in Tables 1 and 2, respectively. It is noted that the value of absorptivity and Marangoni coefficient are calibrated based on the experimental data provided for the track with laser power 195W and scan speed 800 mm/s [35]. These experimental results were provided by NIST to modelers for calibration prior to AM-Bench submission.

As listed in Table 1, the densities at ambient and liquidus temperatures are used for solid and liquid densities, respectively. Values of the density were taken from the literature [43]. To capture more accurate thermal behavior during the process, we used temperature-dependent polynomials for the solid thermal conductivity and solid specific heat capacity as listed in Table 1. The polynomial coefficients were fitted to experimental measurements [43]. An approximate boiling point for the material was used. We used a constant convective heat transfer coefficient to approximate the low-velocity shield gas flow upon the substrate. Emissivity was approximated based on an assumption: for a material in thermodynamic equilibrium, the emissivity is approximately equal to the absorptivity.

Solidification Models

The Kurz-Fisher (KF) model [45] is used to predict the primary dendrite arm spacing (PDAS) λ_p in the process as follows:

$$\lambda_p = A(\Gamma\Delta T_0 D_l/k)^{0.25} G^{-0.5} R^{-0.25} \quad (10)$$

where G represents the magnitude of thermal gradient and R is the solidification rate at the liquid–solid interface of the melt pool, both of which are provided by the thermal process model given in "Thermal-Fluid-Vaporization Model." Here, k is the equilibrium partition coefficient, Γ is the Gibbs–Thomson coefficient, ΔT_0 is the equilibrium freezing range (i.e. the difference between liquidus and solidus temperature), D_l is the liquid diffusivity, and A is a material constant calibrated as 0.98 for IN625 in this study. The parameters used in the model above are summarized in Table 3.

To evaluate the elemental segregation, the Scheil-Gulliver model has been widely used for welding [46] and casting [47]. There are several assumptions in the Scheil-Gulliver model [36]

1. No diffusion in solid phases and infinite diffusion in liquid phases are assumed.
2. Thermodynamic equilibrium exists at the solid-liquid interface.
3. The partition coefficient is a constant.

However, assumptions 2 and 3 are not suitable for additive manufacturing application, because the high cooling rate ($10^3 - 10^6 K/s$) leads to a non-equilibrium

Table 1 Thermo-physical properties of IN625 and process parameters

Name	Property	Value	Reference
Solid density	ρ_s (kg·m^{-3})	8440	[43]
Liquid density	ρ_l (kg·m^{-3})	7640	[43]
Solidus temperature	T_s (K)	1563	[44]
Liquidus temperature	T_l (K)	1623	[44]
Boiling temperature	T_b (K)	3000	-
Solid specific heat capacity	c_{ps} (J ·kg^{-1}·K^{-1})	0.2441T+338.39	[43]
Liquid specific heat capacity	c_{pl} (J ·kg^{-1}·K^{-1})	709.25	[43]
Solid thermal conductivity	k_s (W·m^{-1}·K^{-1})	$0.0163T + 4.5847$	[43]
Liquid thermal conductivity	k_l (W·m^{-1}·K^{-1})	30.078	[43]
Latent heat of fusion	L (kJ·kg^{-1}·K^{-1})	290	[43]
Dynamic viscosity	μ (Pa·s)	7×10^{-3}	[44]
Thermal expansivity	β (1/K)	5×10^{-5}	[44]
Surface tension	γ (N·m^{-1})	1.8	[44]
Marangoni coefficient	$\frac{d\gamma}{dT}$ (N·m^{-1}·K^{-1})	-2×10^{-5} (Calibrated)	-
Emissivity	ε (1)	0.4	-
Absorptivity	η (1)	0.43 (Calibrated)	-
Ambient temperature	T_∞ (K)	295	-
Reference temperature	T_{ref} (K)	295	[43]
Reference density	ρ_{ref} (kg·m^{-3})	7640	-
Convection coefficient	h_c (W·m^{-2}·K^{-1})	10	-
Stefan–Boltzmann constant	σ_s(W ·mm^{-2}K^{-4})	5.67×10^{-14}	[44]

solidification with a non-equilibrium partition coefficient [48]. In this study, a modified microsegregation model [26] for rapid solidification of multicomponent alloys is used as follows. Based on the non-equilibrium condition, the relation between the solute content of the component i in solid, $C^*_{s,i}$, and that in liquid, $C^*_{l,i}$, can be written as

$$C^*_{s,i} = k_{v,i} C^*_{l,i} = k_{v,i} C_{0,i} A_i \tag{11}$$

$$k_{v,i} = \frac{k_i + a_{0,i} R/D_{l,i}}{1 + a_{0,i} R/D_{l,i}} \tag{12}$$

$$A_i = \frac{1}{1 - (1 - k_i) I_v(R\lambda_p/4D_{l,i})} \tag{13}$$

where $C_{0,i}$ is the initial content for each component, $k_{v,i}$ is the partition coefficient of component i, k_i is the equilibrium partition coefficient of component i, $a_{0,i}$ is the length of atomic dimensions of component i, R is the solidification rate computed by the thermal–fluid–vaporization model, $D_{l,i}$ is the solute diffusion coefficient of component i in liquid, and $I_v(\cdot)$ is the Ivantsov function.

By following the mass conservation during the process, the relation between the solute content of the component i in solid, $C^*_{s,i}$, and the volume fraction of solid, f_s, can be derived as [26]

$$C^*_{s,i} = k_{v,i} C_{0,i} A_i (1 - q_i f_s)^{p_i/q_i} \tag{14}$$

$$p_i = k_{v,i} A_i - 1 \tag{15}$$

$$q_i = 1 - 2\alpha'_i k_{v,i} A_i \tag{16}$$

$$\alpha'_i = \alpha_i (1 - \exp(-\frac{1}{\alpha_i})) - \frac{1}{2}\exp(-\frac{1}{2\alpha_i}) \tag{17}$$

$$\alpha_i = \frac{4 D_{s,i} \Delta T_0}{\lambda_p^2 G R} \tag{18}$$

Table 2 Material composition of IN625 by wt%

Material	Ni	C	Mn	Fe	S	Si	Cr	Al	Ti	Co	Mo
IN718	Bal	0.02	0.09	4.31	0.001	0.15	22.25	0.12	0.21	0.1	8.98
Nb	Ta	P									
3.45	0.005	0.009									

Table 3 Parameters used in microstructure models [49]

Name	Property	Value
Equilibrium partition coefficient	k (1)	0.48
Gibbs–Thomson coefficient	Γ ($K \cdot$ m)	3.65×10^{-7}
Equilibrium freezing range	ΔT_0 (K)	60
Liquid diffusion coefficient	D_l ($m^2 \cdot s^{-1}$)	3×10^{-9}
Solid diffusion coefficient	D_s ($m^2 \cdot s^{-1}$)	1×10^{-12}

where $C_{0,i}$ is the initial content for each component as listed in Table 2, $D_{s,i}$ is the solute diffusion coefficient of the component i in solid, and G and R are predicted based on the thermal–fluid–vaporization model. In this study, the concentration of Ni, Cr, Fe, Mo, and Nb for IN625 are predicted (i=Ni, Cr, Fe, Mo, Nb). The parameters used in the microsegregation model are summarized in Tables 3 and 4.

Results and Discussion

The three cases (i.e., case A, case B, and case C mentioned in "Experimental Methods") of a single track laser scan are simulated using an in-house computational thermal–fluid dynamics code called AM-CFD. The computational domain is set to 6×1.2×0.6 mm. A nonuniform structured mesh of 1000×200×100 (total 20 million cells) is used to discretize the domain to obtain a mesh-independent solution. We used fine meshes, $5 \times 3 \times 2\ \mu m$, in the laser scan region. Second order upwind and second order central difference schemes are used for the discretization of the convection and diffusion terms, respectively. The SIMPLE algorithm [51] is used to solve the continuity and momentum equations, and a first-order Backward Euler method is used to discretize the time term. The simulation time is set to 10 ms with a time step of 10 μs. The maximum Courant number is around 2 to 3. The implicit time stepping algorithm used here allows for stable time integration at a Courant number greater than unity [52], and a mesh refinement study varying the Courant number from 0.1 to 10 has been done to verify that the selected mesh size and time step can achieve good convergence and solution stability as well as solution accuracy. The surface profile of melt pool can be then obtained based on the temperature field and input parameters using equation (8, 9). Based on the surface profile, the coordinates of the grid are varied to fit the change of geometry [53]. Finally, the dendrite arm spacing and microsegregation are calculated based on the temperature field. The solution process is repeated at each time step until the residuals satisfy the convergence criterion.

Table 4 Chemical parameters in the microsegregation model [50]

Component	Ni	Cr	Fe	Mo	Nb
Equilibrium partition coefficient k_i	1.03	1.02	1.09	0.85	0.48
Atomic dimension $a_0(nm)$	1.35	1.4	1.45	1.4	1.45

Melt Pool Geometry

The predicted temperature field and streamlines inside the melt pool are displayed in Fig. 2. It is clear that the Marangoni driven flow (i.e., thermocapillary flow) inside the melt pool leads to a strong heat convection. The momentum of liquid metal is lost in the mushy zone because of friction between the formed dendrite and the fluid. The chevron features of solidified materials stem from the fluid flow and free surface evolution.

Figure 3 presents the cross-sectional geometries for cases A, B, and C, in which the melt pool envelopes predicted by the three computational models, i.e. the heat conduction model, thermal-fluid model, and thermal-fluid-vaporization model, are overlapped with the experimental data. It is known that the phenomenon of outward Marangoni flow can lead to a wide and shallow melt pool which highlights the importance of the liquid flow inside the melt pool. As shown in Fig. 3, the depth of the melt pool is overestimated with the heat conduction model, which can not consider heat convection effects. By contrast, the shapes of melt pool predicted using the thermal-fluid model and thermal–fluid–vaporization model are in better agreement with the experimental data as these two models incorporate additional physics. Including the heat loss due to vaporization does not significantly affect the shape of the melt pool, but reduces both its depth and width, which leads to a better prediction of melt pool geometry as compared with the experimental results.

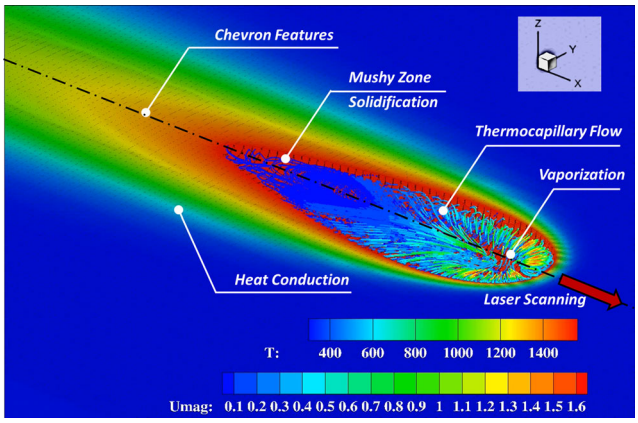

Fig. 2 Temperature and streamlines in the melt pool for AM-Bench case B: laser power 195W, scan speed 800mm/s. The physical phenomena considered in the model are marked

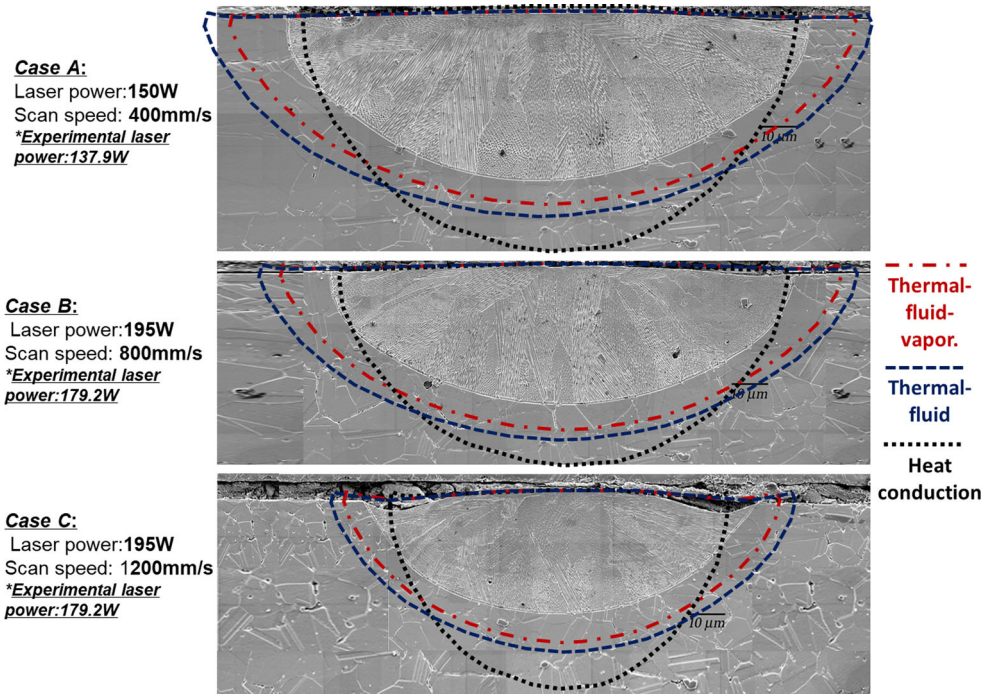

Fig. 3 Experimental cross-sectional geometries in the three cases. The corresponding melt pool boundary (solidus temperature) predicted by thermal-fluid-vaporization model (red dashed dotted line), thermal-fluid model (blue dashed line), and heat conduction model (black dotted line) are overlaid on the experimental images for representation. Experimental images are released from the AM-Bench committee [54]

The melt pool length for the three cases is summarized in Table 5. It is shown that for cases B and C, the results from the thermal–fluid–vaporization model agree well with the experimental data, with a difference that is smaller than the experimental uncertainty. For case A, a 24% difference of melt pool length is obtained. The heat conduction model, ignoring both the fluid flow and vaporization, also predicts the melt pool length well. It is noted that the heat conduction and thermal–fluid model provide similar predictions of the melt pool length. This may be because the scan speed (400–1200 mm/s) is comparable with the thermocapillary flow velocity (< 1600 mm/s); thus, the melt pool length is mainly dominated by the heat source moving rather than the flow convection inside the melt pool. The difference between the simulation and experimental results of the melt pool size is mainly attributed to both the simplified assumptions in the computation models and the lack of accurate thermophysical properties of the material.

Cooling Rate

Cooling rate, the rate at which temperature decreases with time, is an important factor in additive manufacturing. The cooling process from liquidus to solidus temperature has a large influence on dendrite arm spacing, grain structure, microsegregation, and hot cracking, while the process of cooling from solidus temperature to a given temperature, e.g., recrystallization temperature (approximate 1000 °C for IN625 [55]), affects solid-state phase transformation, residual stress, and grain coarsening. As shown in Fig. 4,

Table 5 Comparison of melt pool length between experiments and three computational models: thermal-fluid-vaporization, thermal-fluid, and heat conduction model

	Length (μm) measured by experiments	Length (μm) predicted by thermal-fluid-vapor. model	Length (μm) predicted by thermal-fluid model	Length (μm) predicted by heat conduction model
Case	Value	Value (difference)	Value (difference)	Value (difference)
A: 150W, 400 mm/s	659 ± 21	502 (24%)	542 (18%)	564 (14%)
B: 195W, 800 mm/s	782 ± 21	772 (1%)	843 (8%)	883 (13%)
C: 195W, 1200 mm/s	754 ± 46	717 (5%)	785 (4%)	832 (10%)

Experimental data has been released by the AM-Bench committee [54]

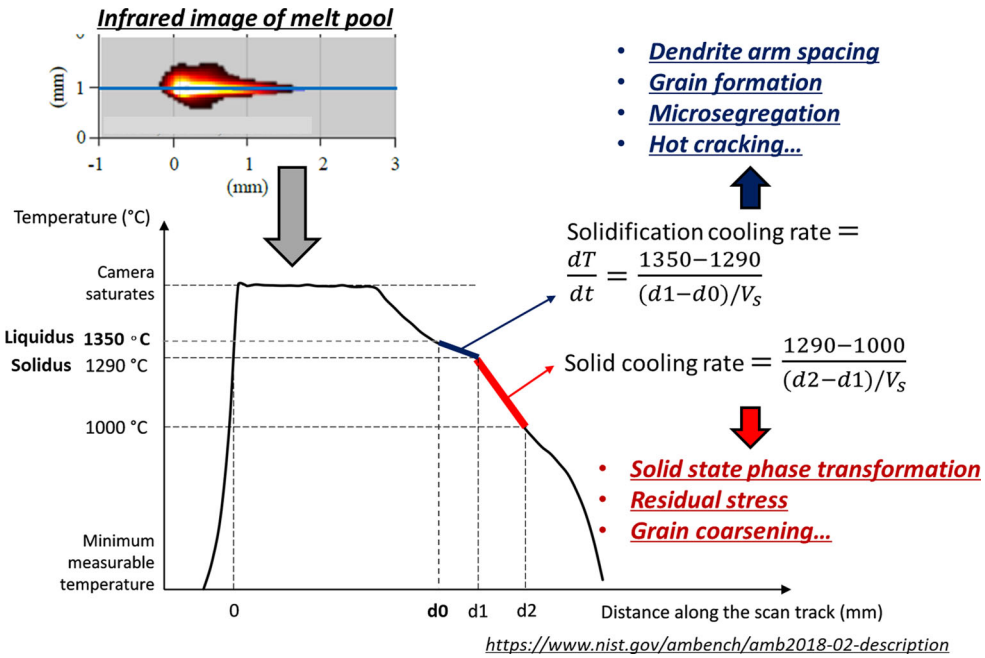

Fig. 4 Definitions of cooling rates. Temperature curve along the centerline of scan track can be obtained from experimental infrared images. Two cooling rates, i.e. solidification cooling rate and solid cooling rate, with different temperature ranges are defined. They are related to various physical phenomena in additive manufacturing

the cooling rates at these two different stages are referred to as solidification cooling rate and solid cooling rate, respectively, both of which are defined as follows.

$$\text{Solidification cooling rate} = \frac{T_{liq} - T_{solid}}{\Delta t} = \frac{T_{liq} - T_{solid}}{(d_{liq} - d_{solid})/V_s} \tag{19}$$

$$\text{Solid cooling rate} = \frac{T_{solid} - 1000°\text{C}}{\Delta t'} = \frac{T_{solid} - 1000°\text{C}}{(d_{solid} - d_{1000})/V_s} \tag{20}$$

where T_{liq} is the liquidus temperature, T_{solid} is the solidus temperature, Δt is the cooling time interval determined by dividing the distance between liquidus and solidus isotherms $d_{liq} - d_{solid}$ by the scan speed V_s, and $\Delta t'$ is determined by dividing the distance between the solidus temperature and 1000 °C by the scan speed.

The cooling rates for the three cases are shown in Fig. 5. Results from the three thermal models mentioned in "Computational Models" (i.e., heat conduction model, thermal-fluid model, and thermal–fluid–vaporization model)

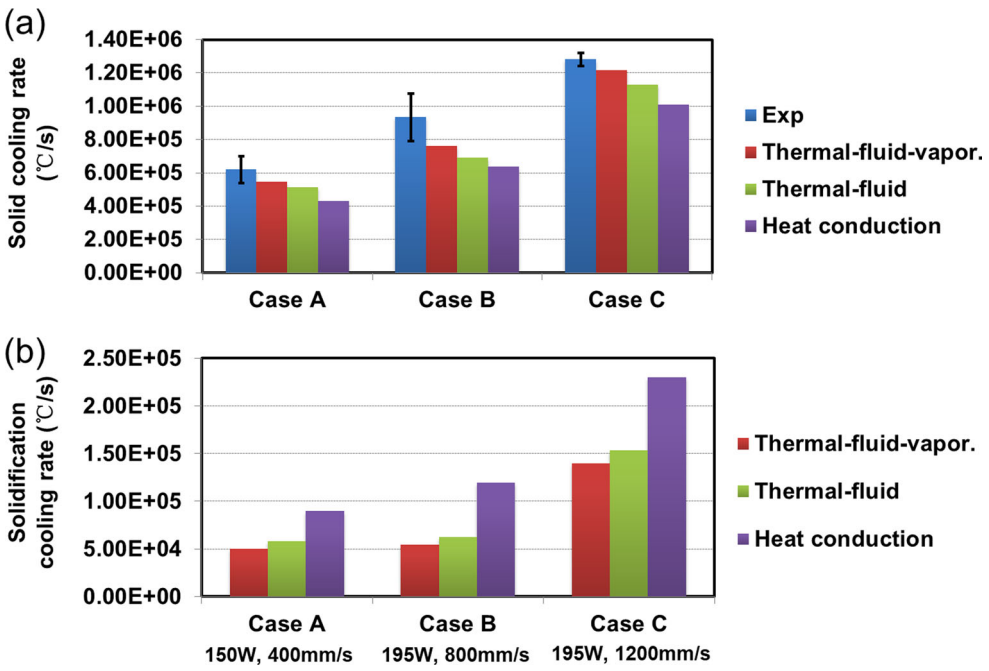

Fig. 5 Comparisons of cooling rates between experiments and three models, i.e. the heat conduction model, thermal-fluid model, and thermal-fluid-vaporization model: **a** solid cooling rate, **b** solidification cooling rate. Experimental data is released by the AM-Bench Committee [54]

Table 6 Comparison of solid cooling rate between experiments and three computational models: thermal-fluid-vaporization model, thermal-fluid model, and heat conduction model

	Experimental solid cooling rate (K/s)	Solid cooling rate of thermal-fluid-vapor. (K/s)	Solid cooling rate of thermal-fluid (K/s)	Solid cooling rate of heat conduction (K/s)
Case	Value	Value (difference)	Value (difference)	Value (difference)
A: 150W, 400 mm/s	$6.20 \pm 0.799 \times 10^5$	5.44×10^5 (12%)	5.11×10^5 (18%)	4.3×10^5 (31%)
B: 195W, 800 mm/s	$9.35 \pm 1.43 \times 10^5$	7.59×10^5 (19%)	6.89×10^5 (26%)	6.35×10^5 (32%)
C: 195W, 1200 mm/s	$12.8 \pm 3.94 \times 10^5$	12.14×10^5 (5%)	11.3×10^5 (12%)	10.1×10^5 (21%)

Experimental data is released by the AM-Bench Committee [54]

are compared with the experimental data. As shown in Fig. 5a, results from the thermal–fluid–vaporization model provide the best agreement with the experimental data. The prediction for case A falls exactly within the range of experimental data. Quantification between experimental and simulation results are listed in Table 6. The prediction results from the thermal–fluid model without vaporization are out of the range of experimental results and have a 12 to 26% discrepancy in solid cooling rate. The results from the heat conduction model have discrepancies as high as 30%. In addition, the simulated solidification cooling rates are compared in Fig. 5b and Table 7. Since it is still challenging to directly measure the solidification cooling rate, only the solid cooling rate results were measured in AM-Bench using infrared imaging (detailed descriptions of the measurements can be found in reference [56]). When compared with the thermal–fluid–vaporization model, it is observed that neglecting physical mechanisms in the melt pool leads to differences in the range of 10 to 16% for the thermal–fluid model and 64 to 118% for the heat conduction model. The above results indicate that analyzing thermal evolution during AM using the thermal conduction model, ignoring fluid flow and vaporization, underestimates the solid cooling rate and considerably overestimates the solidification cooling rate.

To show the effects of fluid flow and vaporization on the spatial temperature distribution, temperature profiles along the scan track are extracted from the simulation results and plotted in Fig. 6. It is clear that a significant difference occurs above the solidus temperature, and this difference gradually decreases as the temperature falls below the solidus temperature. Additionally, unrealistic peak temperatures of 10777 °C from heat the conduction model and 5452 °C from the thermal–fluid model are reached; these temperatures are much higher than the boiling point of IN625 (2727 °C) and cause large changes in the solidification cooling rate. From these tests, it can be observed that both the thermal convection and vaporization are the essential mechanisms in the thermal analysis. An inaccurate estimation of the cooling rate is expected if these mechanisms are not properly accounted for.

Surface Topography

In this section, the 3D topography of the top surface is studied. The quantifiable 3D surface features include chevron geometries and spacing as well as height distribution perpendicular to the laser track.

Figure 7 shows the surface topography for the three cases. The experimental profiles were obtained using

Table 7 Comparison of solidification cooling rate between three computational models: thermal-fluid-vaporization model, thermal-fluid model, and heat conduction model

	Solidification cooling rate of thermal-fluid-vapor. (K/s)	Solidification cooling rate of thermal-fluid (K/s)	Solidification cooling rate of heat conduction (K/s)
Case	Value	Value (difference)	Value (difference)
A: 150W, 400 mm/s	5.0×10^4	5.8×10^4 (16%)	9.0×10^4 (80%)
B: 195W, 800 mm/s	5.5×10^4	6.3×10^4 (15%)	12×10^4 (118%)
C: 195W, 1200 mm/s	14×10^4	15.4×10^4 (10%)	23×10^4 (64%)

The reported difference is the difference between the thermal-fluid-vapor model and subsequent models

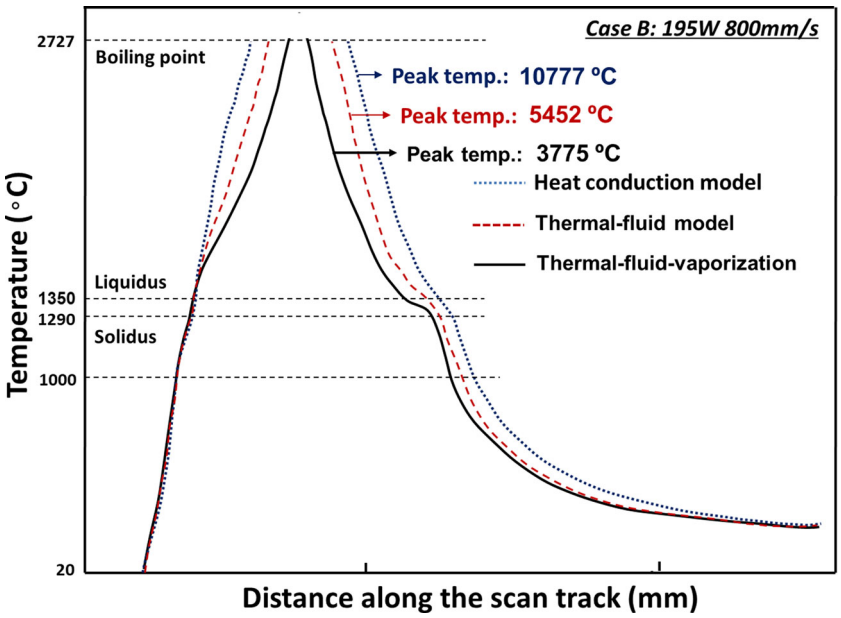

Fig. 6 Comparison of temperature curves for case B (195 W, 800 mm/s) between three models: heat conduction model, thermal-fluid model, and thermal-fluid-vaporization model

scanning laser confocal microscopy and the simulation results, which show good agreement with the experiments, are from the thermal-fluid-vaporization model. Chevron formations are clearly observed in the predictions. They are formed at the mushy zone at the tail of the melt pool and thus correlated to the melt pool boundary. Chevron spacing and angle, defined in Fig. 8, are calculated over the length of the scan track. The average, maximum, and minimum

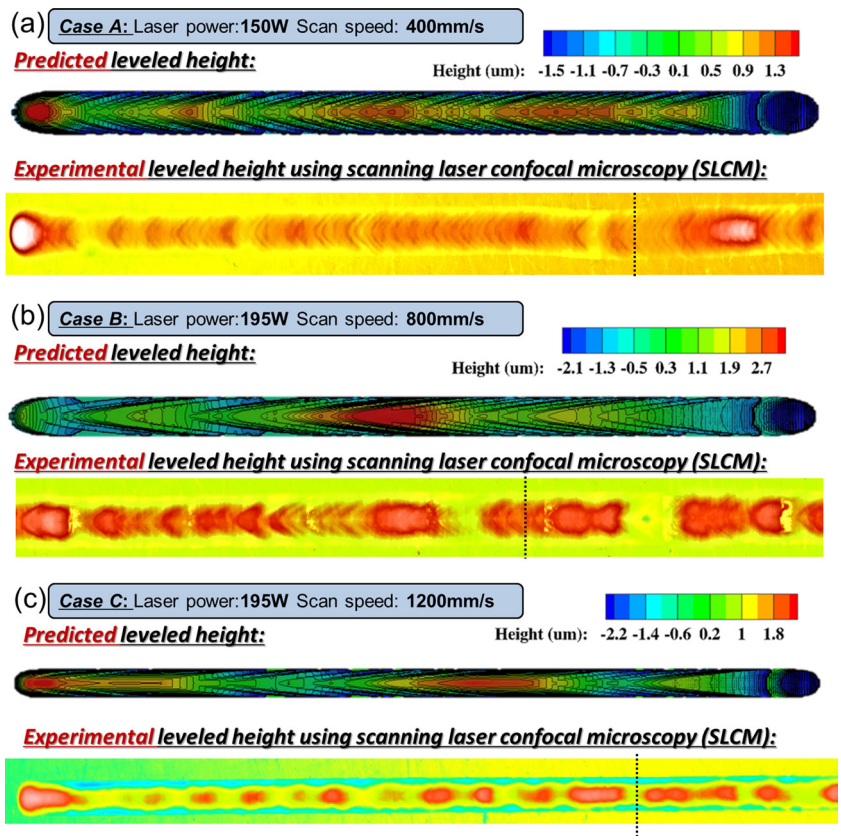

Fig. 7 Predicted and experimental surface topographies of the three cases: **a** 150 W, 400 mm/s, **b** 195 W, 800 mm/s, **c** 195 W, 1200 mm/s. Experimental data is released by the AM-Bench Committee [54]

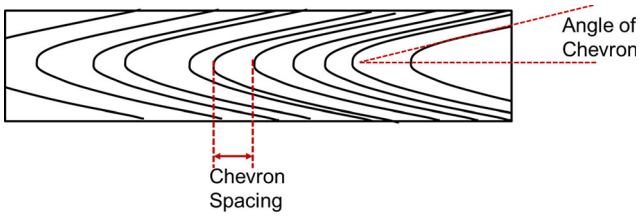

Fig. 8 Definition of chevron angle and chevron spacing

values of them are tabulated in Table 8. It is found that the chevron spacing increases with the increase of scan speed, approximately following the relationship:

$$L = \frac{V_s \lambda}{c} \tag{21}$$

where L is the chevron spacing, λ is the wave length of the flow in the melt pool, and c is the wave velocity equal to the fluid velocity at the surface of the melt pool. Based on the water wave theory [57], the wave length and wave velocity are expressed as

$$\frac{c}{(gH)^{1/2}} = f\left(\frac{\lambda}{H}, \frac{\gamma}{\rho g \lambda^2}\right) \tag{22}$$

where H is depth of the melt pool and γ is surface tension. We assume that λ, γ, and H are essentially the same in the three cases. As a result, the chevron spacing L is approximately proportional to the scan speed V_s. In addition, the chevron angle decreases with the increase of scan speed as shown in Table 8. This trend is caused by the fact that the teardrop shape of the melt pool is elongated as the scan speed increases.

Figure 9 shows the surface height along the width of the solidified track for the three cases. The experimental data shown in Fig. 9b, d, and f were extracted along specific transverse lines as shown in Fig. 7 marked out by the dashed lines, while the average, minimum, and maximum leveled height curves across the solidified track length plotted in Fig. 9a, c, and e are obtained from the result of the thermal-fluid-vaporization model. It is found that the experimental data falls in the range of the maximum and minimum values of the simulation results, indicating a good agreement. It is noted that instead of using an interface capturing method such as Volume of Fluid (VOF), in which the accuracy of the free surface capturing depends on the size of fixed grids near the free surface, we used a modified semi-analytical method by minimizing the total surface energy equation (8) to obtain the deformation of the free surface [58]. Then, the grid coordinates are updated to fit the deviation of melt pool surface using a moving mesh framework [53]. Thus, the calculation of the height excursion is independent of the mesh resolution in the z direction, because the value of the height excursion is directly obtained by solving equation (8).

Table 8 Predicted spacing, angle, and height deviation of chevron features for the three cases

Case	A	B	C
Chevron spacing, mean (μm)	78	148	187
Chevron spacing, std. dev. (μm)	31	48	87
Chevron angle, mean (°)	27	16	12
Chevron spacing, std. dev. (°)	5	4	2
Height excursion (max–min) (μm)	3	5.3	4.6

Dendritic Microstructure

In this section, PDAS and elemental microsegregation are studied. The combination of the magnitude of thermal gradient G and solidification rate R around the liquid-solid interface plays an important role in determining the solidification modes and grain morphology [59] as illustrated in Fig. 10.

Rather than resolving the detailed grain structure, the PDAS as defined in Fig. 10 is predicted using G and R from the thermal–fluid–vaporization model and compared with experimental data. In order to perform the comparison, G and R are first projected onto a cross section of the track (as seen in Fig. 11a and b, respectively, for case B). Then, according to Eq. 10, a contour of the PDAS distribution over the cross section is plotted in Fig. 11c showing a nonuniform PDAS field corresponding to the distribution of G and R. It is found that the predicted PDAS has a maximum of 0.79 μm in this case located at the center of the cross-section and a minimum of 0.23 μm near the periphery of the cross-section. This trend is validated by a sample of eight experimental measurements as shown in Fig. 11d. The experimental PDAS decreases from the center to the periphery of the cross section of the sample. The maximum and minimum values of PDAS are presented in Fig. 12 for all three cases, demonstrating a good agreement with experimental results. Another conclusion we can draw from the comparison in Fig. 12 is that the PDAS decreases with the increase of scan speed due to higher solidification rates leading to finer dendrites.

To estimate the microsegregation between dendrite arms, the non-equilibrium model [26] described in "Solidification Models" is used to predict the concentration profiles.

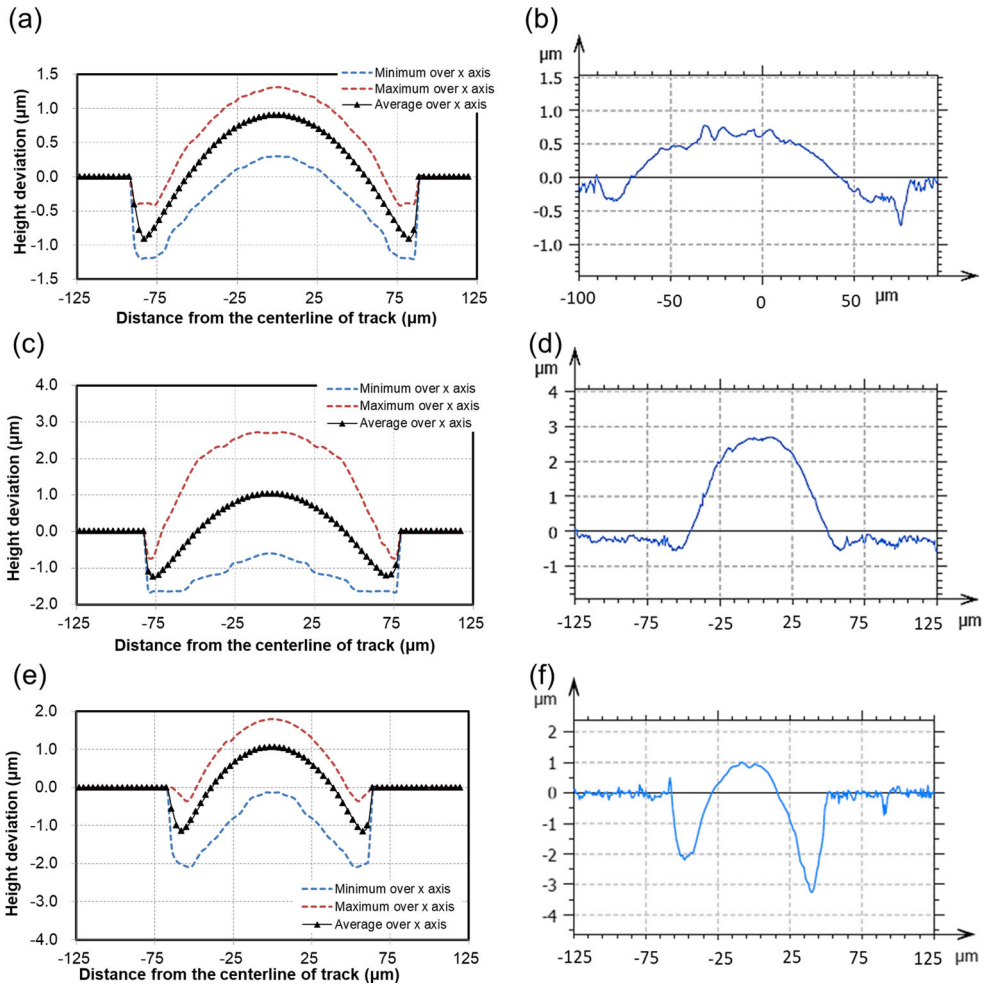

Fig. 9 Comparison of height profiles between experimental measurements and predicted results: **a**, **c**, and **e**: predicted results of minimum, maximum, and average height profiles over the x axis (scan direction) as a function of transverse direction distance (perpendicular to the scan direction) for case A, case B, and case C, respectively; **b**, **d**, and **f**: experimental results of height profile along specific transverse lines shown in Fig. 7 (the dashed lines) for case A, case B, and case C, respectively. Experimental data comes from [54]

Figure 13 shows the concentration profiles, where the results from the Scheil-Gulliver model [37] are also presented for comparison. It is observed that the concentration profiles calculated by the non-equilibrium model better approximate the actual additive manufacturing process, i.e., a rapid solidification process with relatively low microsegregation.

To quantify the degree of microsegregation, the segregation range ΔC for each element is defined as

$$\Delta C = \frac{C_{solid} - C_{liquid}}{C_{liquid}} \tag{23}$$

where C_{liquid} is the concentration at the beginning of solidification ($f_s = 0$), and C_{solid} is the concentration when

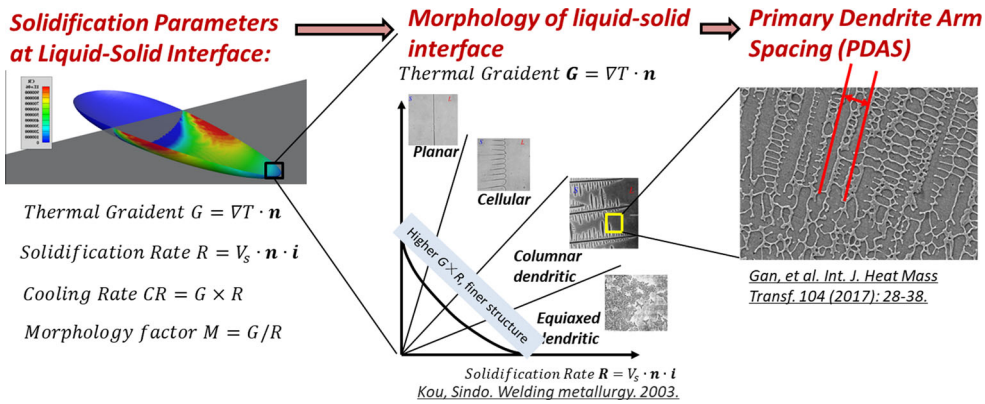

Fig. 10 Schematic of effect of thermal behavior on dendritic microstructure [27, 59]

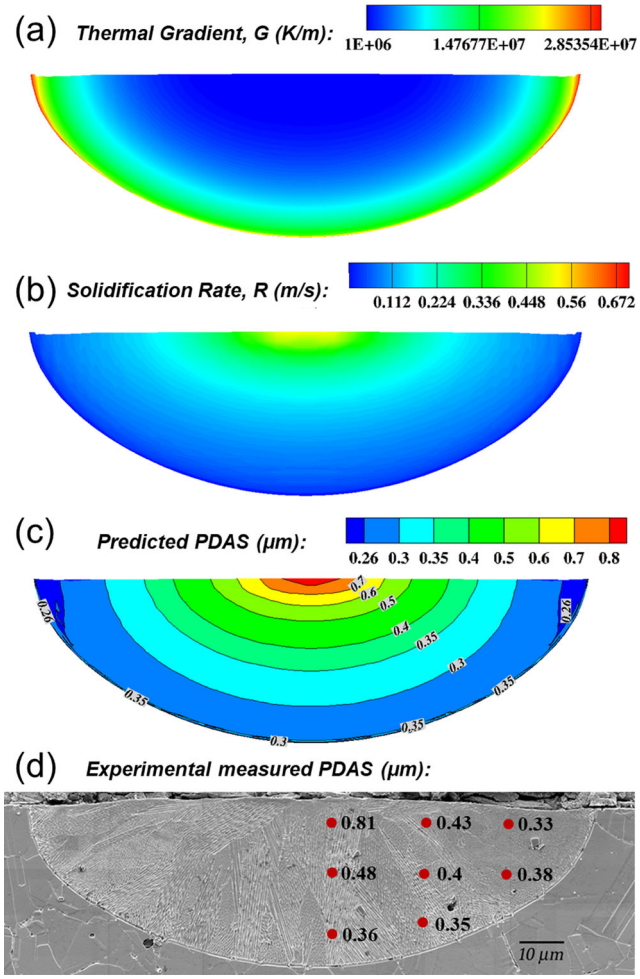

Fig. 11 Spatial distribution of **a** thermal gradient, **b** solidification rate, **c** predicted PDAS, and **d** experimentally measured PDAS at the cross-section for case B (195 W, 800 mm/s). Experimental data is released by the AM-Bench Committee [54]

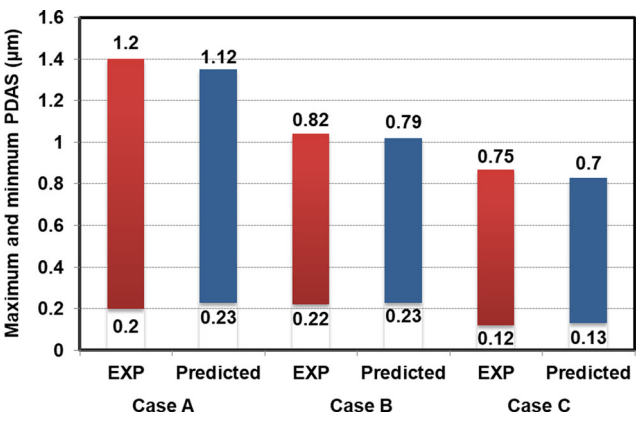

Fig. 12 Comparisons of maximum and minimum PDAS between experimental and predicted results for the three cases. Experimental data is released by the AM-Bench Committee [54]

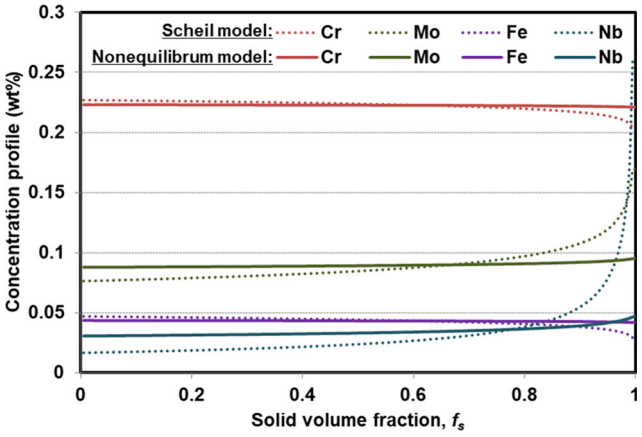

Fig. 13 Comparison of concentration profile between Scheil-Gulliver model and non-equilibrium model for case B: 195 W, 800 mm/s

the solidification is completed ($f_s = 1$). For the primary elements Ni, Cr, Mo, Fe, and Nb, ΔC can be calculated from the concentration profiles, such as Fig. 13, and presented in Fig. 14 for the three cases. Figure 14 demonstrates that the elements Ni, Cr, and Fe are depleted between the dendrite arms after the solidification and Mo and Nb are enriched in the interdendritic regions. The enriched interdendritic Nb and Mo have also been observed in the experimental measurements [50]. In addition, the segregation ranges of all elements decrease from case A to C (increasing scan speed) as shown in Fig. 14. For example, the segregation range of Nb decreases from 56.8% in case A to 40.6% in case C. Given that severe elemental microsegregation increases the susceptibility of hot cracking and degrades the mechanical properties of solidified parts [60], increasing scan speed causes higher cooling rate/solidification rate and may be beneficial for the improvement of mechanical properties of the manufactured materials.

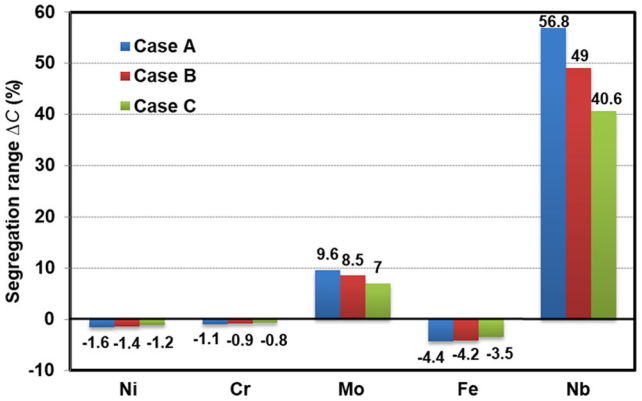

Fig. 14 Comparisons of segregation ranges of elements for the three cases predicted by the numerical simulation

Conclusions

In this work, a framework of integrated models is proposed for the simulation of additive manufacturing. Through comparisons with AM-Bench tests on laser melting of Inconel 625 plate with three different combinations of scan speed and laser power, the melt pool geometry, cooling rate, surface topography of laser track, primary dendrite arm spacing, and elemental microsegragation are studied. From this work, we concluded:

1. Including fluid flow and heat loss due to vaporization in the heat conduction model can significantly improve the prediction accuracy of thermal analysis. The simulation results from the model with fluid flow and vaporization are in good agreement with the experimental data on the melt pool geometry (width and depth), solidification cooling rate, and solid cooling rate.
2. Neglecting heat loss due to vaporization underestimates solid cooling rate by approximately 10% and overestimates solidification cooling rate by 15%, respectively. Neglecting both vaporization and fluid flow results in a 20% underestimation in the solid cooling rate and a nearly 100% overestimation in the solidification cooling rate.
3. Melt pool length predicted by both the heat conduction model, thermal-fluid model and thermal-fluid-vaporization model can match the experimental measurements.
4. Surface topographies of tracks can be qualitatively predicted by minimizing the total energy of surface. Clear chevron features are found in all three cases. An increase in scan speed leads to a increase of the chevron spacing but a decrease of the chevron angle.
5. The primary dendrite arm spacing can be successfully predicted using the Kurz-Fisher (KF) model with accurate thermal gradient G and solidification rate R.
6. Concentration profiles with lower microsegregation are predicted by a non-equilibrium solidification model as compared with the well-known Scheil-Gulliver model. The increase of scan speed inhibits the elemental microsegregation.

Acknowledgements G. J. Wagner and W. K. Liu acknowledge the support by the National Science Foundation (NSF) Cyber-Physical Systems (CPS) under grant No. CPS/CMMI-1646592. G. J. Wagner and W. K. Liu acknowledge the support by the Digital Manufacturing and Design Innovation Institute (DMDII) through award number 15-07. W. K. Liu and Z. Gan acknowledge the support by Center for Hierarchical Materials Design (CHiMaD) under grant No. 70NANB14H012. W. K. Liu acknowledges the support of NSF grant CMMI-1762035. Y. Lian acknowledges the support by BIT Teli Young Fellow Recruitment Program. S. Lin acknowledges the support by the NSF Graduate Research Fellowship under Grant No. DGE-1324585. K. Jones acknowledge the support by the Murphy Fellowship from Northwestern University. We extend our thanks to Dr. Lyle Levine, Dr. Brandon Lane, and the AM-Bench committee for their work and leadership in providing this valuable forum for the AM research community.

Compliance with Ethical Standards

Conflict of interest The authors declare that they have no conflict of interest.

References

1. DebRoy T, Wei H, Zuback J, Mukherjee T, Elmer J, Milewski J, Beese A, Wilson-Heid A, De A, Zhang W (2017) Additive manufacturing of metallic components – process, structure and properties. Prog Mater Sci 92:112–224
2. Keller T, Lindwall G, Ghosh S, Ma L, Lane BM, Zhang F, Kattner UR, Lass EA, Heigel JC, Idell Y et al (2017) Application of finite element, phase-field, and CALPHAD-based methods to additive manufacturing of Ni-based superalloys. Acta Mater 139:244–253
3. Gan Z, Yu G, Li S, He X, Chen R, Zheng C, Ning W (2016) A novel intelligent adaptive control of laser-based ground thermal test. Chin J Aeronaut 29:1018–1026
4. King WE, Barth HD, Castillo VM, Gallegos GF, Gibbs JW, Hahn DE, Kamath C, Rubenchik AM (2014) Observation of keyhole-mode laser melting in laser powder-bed fusion additive manufacturing. J Mater Process Technol 214:2915–2925
5. Pyka G, Burakowski A, Kerckhofs G, Moesen M, Van Bael S, Schrooten J, Wevers M (2012) Surface modification of ti6al4v open porous structures produced by additive manufacturing. Adv Eng Mater 14:363–370
6. AlMangour B, Yang J-M (2016) Improving the surface quality and mechanical properties by shot-peening of 17-4 stainless steel fabricated by additive manufacturing. Mater Des 110:914–924
7. Chen Y, Zhang K, Huang J, Hosseini SRE, Li Z (2016) Characterization of heat affected zone liquation cracking in laser additive manufacturing of Inconel 718. Mater Des 90:586–594
8. Formenti A, Eliasson A, Mitchell A, Fredriksson H (2005) Solidification sequence and carbide precipitation in Ni-base superalloys in718, in625 and in939. High Temp Mater Process 24:239–258
9. Smith J, Xiong W, Yan W, Lin S, Cheng P, Kafka OL, Wagner GJ, Cao J, Liu WK (2016) Linking process, structure, property, and performance for metal-based additive manufacturing: computational approaches with experimental support. Comput Mech 57:583–610
10. Emamian A, Alimardani M, Khajepour A (2012) Correlation between temperature distribution and in situ formed microstructure of Fe–tic deposited on carbon steel using laser cladding. Appl Surf Sci 258:9025–9031
11. Gao W, Zhao S, Wang Y, Zhang Z, Liu F, Lin X (2016) Numerical simulation of thermal field and Fe-based coating doped Ti. Int J Heat Mass Transf 92:83–90
12. Smith J, Xiong W, Cao J, Liu WK (2016) Thermodynamically consistent microstructure prediction of additively manufactured materials. Comput Mech 57:359–370
13. Mukherjee T, Wei H, De A, DebRoy T (2018) Heat and fluid flow in additive manufacturing—Part I: modeling of powder bed fusion. Comput Mater Sci 150:304–313

14. Mukherjee T, Wei H, De A, DebRoy T (2018) Heat and fluid flow in additive manufacturing—Part II: powder bed fusion of stainless steel, and titanium, nickel and aluminum base alloys. Comput Mater Sci 150:369–380
15. Knapp G, Mukherjee T, Zuback J, Wei H, Palmer T, De A, DebRoy T (2017) Building blocks for a digital twin of additive manufacturing. Acta Mater 135:390–399
16. Qi H, Mazumder J, Ki H (2006) Numerical simulation of heat transfer and fluid flow in coaxial laser cladding process for direct metal deposition. J Appl Phys 100:024903
17. Wen S, Shin YC (2011) Modeling of the off-axis high power diode laser cladding process. J Heat Trans 133:031007
18. King WE, Anderson AT, Ferencz R, Hodge N, Kamath C, Khairallah SA, Rubenchik AM (2015) Laser powder bed fusion additive manufacturing of metals; physics, computational, and materials challenges. Appl Phys Rev 2:041304
19. Panwisawas C, Qiu C, Anderson MJ, Sovani Y, Turner RP, Attallah MM, Brooks JW, Basoalto HC (2017) Mesoscale modelling of selective laser melting: thermal fluid dynamics and microstructural evolution. Comput Mater Sci 126:479–490
20. Khairallah SA, Anderson AT, Rubenchik A, King WE (2016) Laser powder-bed fusion additive manufacturing: physics of complex melt flow and formation mechanisms of pores, spatter, and denudation zones. Acta Mater 108:36–45
21. Yan W, Ge W, Qian Y, Lin S, Zhou B, Liu WK, Lin F, Wagner GJ (2017) Multi-physics modeling of single/multiple-track defect mechanisms in electron beam selective melting. Acta Mater 134:324–333
22. Lian Y, Lin S, Yan W, Liu WK, Wagner GJ (2018) A parallelized three-dimensional cellular automaton model for grain growth during additive manufacturing. Comput Mech 61:543–558
23. Rodgers TM, Madison JD, Tikare V (2017) Simulation of metal additive manufacturing microstructures using kinetic monte carlo. Comput Mater Sci 135:78–89
24. Kundin J, Mushongera L, Emmerich H (2015) Phase-field modeling of microstructure formation during rapid solidification in inconel 718 superalloy. Acta Mater 95:343–356
25. Dantzig JA, Rappaz M (2009) Solidification. EPFL Press
26. Liang Y-J, Cheng X, Wang H-M (2016) A new microsegregation model for rapid solidification multicomponent alloys and its application to single-crystal nickel-base superalloys of laser rapid directional solidification. Acta Mater 118:17–27
27. Gan Z, Yu G, He X, Li S (2017) Numerical simulation of thermal behavior and multicomponent mass transfer in direct laser deposition of Co-base alloy on steel. Int J Heat Mass Transf 104:28–38
28. Parimi LL, Ravi G, Clark D, Attallah MM (2014) Microstructural and texture development in direct laser fabricated in718. Mater Charact 89:102–111
29. Murr LE, Gaytan S, Ceylan A, Martinez E, Martinez J, Hernandez D, Machado B, Ramirez D, Medina F, Collins S et al (2010) Characterization of titanium aluminide alloy components fabricated by additive manufacturing using electron beam melting. Acta Mater 58:1887–1894
30. Heigel JC, Lane BM (2018) Measurement of the melt pool length during single scan tracks in a commercial laser powder bed fusion process. J Manuf Sci Eng 140:051012
31. Ghosh S, Ma L, Levine LE, Ricker RE, Stoudt MR, Heigel JC, Guyer JE (2018) Single-track melt-pool measurements and microstructures in inconel 625. JOM, 1–6
32. Escano LI, Parab ND, Xiong L, Guo Q, Zhao C, Fezzaa K, Everhart W, Sun T, Chen L (2018) Revealing particle-scale powder spreading dynamics in powder-bed-based additive manufacturing process by high-speed x-ray imaging. Sci Rep 8:15079
33. Zhao C, Fezzaa K, Cunningham RW, Wen H, Carlo F, Chen L, Rollett AD, Sun T (2017) Real-time monitoring of laser powder bed fusion process using high-speed x-ray imaging and diffraction. Sci Rep 7:3602
34. Lyle BL, Levine E (2018) AM-Bench 2018. https://www.nist.gov/ambench/
35. Lyle BL, Levine E (2018) Ambench2018-description. https://www.nist.gov/ambench/amb2018-02-description/
36. Kurz W, Fisher DJ (1986) Fundamentals of solidification, vol 1. trans tech publications Aedermannsdorf, Switzerland
37. Gulliver G (1922) Metal and alloys
38. Gan Z, Liu H, Li S, He X, Yu G (2017) Modeling of thermal behavior and mass transport in multi-layer laser additive manufacturing of ni-based alloy on cast iron. Int J Heat Mass Transfer 111:709–722
39. Gan Z, Yu G, He X, Li S (2017) Surface-active element transport and its effect on liquid metal flow in laser-assisted additive manufacturing. Int Commun Heat Mass Transfer 86:206–214
40. Bennon W, Incropera F (1987) A continuum model for momentum, heat and species transport in binary solid-liquid phase change systems—I. Model formulation. Int J Heat Mass Transf 30:2161–2170
41. He X, DebRoy T, Fuerschbach P (2003) Alloying element vaporization during laser spot welding of stainless steel. J Phys D Appl Phys 36:3079
42. Cho W-I, Na S-J, Cho M-H, Lee J-S (2010) Numerical study of alloying element distribution in CO_2 laser–GMA hybrid welding. Comput Mater Sci 49:792–800
43. Capriccioli A, Frosi P (2009) Multipurpose ANSYS Fe procedure for welding processes simulation. Fusion Eng Des 84:546–553
44. Pawel R, Williams R (1985) Survey of physical property data for several alloys, Technical Report, Oak Ridge National Lab.
45. Kurz W, Fisher D (1981) Dendrite growth at the limit of stability: tip radius and spacing. Acta Metall 29:11–20
46. Lippold J, Sowards J, Murray G, Alexandrov B, Ramirez A (2008) Weld solidification cracking in solid-solution strengthened Ni-base filler metals. In: Hot cracking phenomena in welds II. Springer, pp 147–170
47. Pudar M, Zamberger S, Spiradek-Hahn K, Radis R, Kozeschnik E (2010) Computational analysis of precipitation during continuous casting of microalloyed steel. Steel Res Int 81:372–380
48. Tian Y, McAllister D, Colijn H, Mills M, Farson D, Nordin M, Babu S (2014) Rationalization of microstructure heterogeneity in inconel 718 builds made by the direct laser additive manufacturing process. Metall and Mater Trans A 45:4470–4483
49. Ghosh S, Ma L, Ofori-Opoku N, Guyer JE (2017) On the primary spacing and microsegregation of cellular dendrites in laser deposited Ni–Nb alloys. Modell Simul Mater Sci Eng 25:065002
50. Hu Y, Lin X, Yu X, Xu J, Lei M, Huang W (2017) Effect of Ti addition on cracking and microhardness of Inconel 625 during the laser solid forming processing. J Alloys Compd 711:267–277
51. Patankar S (1980) Numerical heat transfer and fluid flow. CRC Press
52. Shepherd J (2002) Overcoming the CFL time-step limitation: a stable iterative implicit numerical scheme for slowly evolving advection-diffusion systems. Ocean Model 4:17–28
53. Tuković Ž, Jasak H (2012) A moving mesh finite volume interface tracking method for surface tension dominated interfacial fluid flow. Comput Fluids 55:70–84
54. Lyle BL, Levine E (2018) AM-Bench 2018-test-data. https://www.nist.gov/ambench/benchmark-test-data/
55. Zhao D, Chaudhury P, Frank R, Jackman L (1994) Flow behavior of three 625-type alloys during high temperature deformation. In: Superalloys 718,625,706 and Various Derivatives. The Minerals, Metals & Materials Society, pp 625–706

56. Heigel JC, Lane BM (2017) The effect of powder on cooling rate and melt pool length measurements using in situ thermographic techniques. In: Solid freeform fabrication 2017
57. Tan Q-M (2011) Dimensional analysis: with case studies in mechanics. Springer Science & Business Media
58. Zhang W, Kim C-H, DebRoy T (2004) Heat and fluid flow in complex joints during gas metal arc welding—Part I: Numerical model of fillet welding. J Appl Phys 95:5210–5219
59. Kou S (2003) Welding metallurgy. New Jersey, pp 431–446
60. Abbaschian L, Lima MSFd (2003) Cracking susceptibility of aluminum alloys during laser welding. Mater Res 6:273–278